





## The underexposed effect of elastic electron collisions in dusty plasmas

Tim Jacobus Adrianus Staps <sup>1</sup>, Marvin Igor van de Ketterij <sup>1</sup>, Bart Platier <sup>1</sup> & Job Beckers <sup>1</sup>

Dusty plasmas comprise a complex mixture of neutrals, electrons, ions and dust grains, which are found throughout the universe and in many technologies. The complexity resides in the chemical and charging processes involving dust grains and plasma species, both of which impact the collective plasma behavior. For decades, the orbital-motion-limited theory is used to describe the plasma charging of dust grains, in which the electron current is considered collisionless. Here we show that the electron (momentum transfer) collision frequency exceeds the electron plasma frequency in a powder-forming plasma. This indicates that the electron current is no longer collisionless, and the orbital-motion-limited theory may need corrections to account for elastic electron collisions. This implication is especially relevant for higher gas pressure, lower plasma density, and larger dust grain size and density.

<sup>1</sup>Department of Applied Physics, Eindhoven University of Technology, Eindhoven, The Netherlands. ✉email: [t.j.a.staps@tue.nl](mailto:t.j.a.staps@tue.nl)

Complex and dusty plasmas are ubiquitous throughout outer space (where they dictate astrophysical and astrochemical processes), in laboratories worldwide (as macroscopic model systems to study fundamental physical phenomena), and in industries (where they form the backbone of many manufacturing processes). For instance, extraterrestrial dust grains—often embedded in (partly) ionized media called plasmas—may play a critical role in interstellar space<sup>1,2</sup>, in planet and star formation<sup>3–5</sup>, and even in the emergence of life<sup>6,7</sup>. At the same time, the origin of cosmic dust<sup>8</sup> and its interplay with other cosmic constituents<sup>9,10</sup> remains largely elusive. Closer to home, cosmic dust analogs are created on a daily basis in laboratory dusty plasmas<sup>11</sup> to study phase transitions at macroscopic length scales, fundamental plasma charging dynamics<sup>12,13</sup>, strongly coupled systems<sup>14</sup>, and the crystallization of lattice structures<sup>15</sup>. In the semiconductor and solar cell industry, low-temperature plasmas are indispensable for the formation of thin, uniform layers, such as coatings. The chemically reactive plasmas used for such applications have appeared more than once as breeding grounds for particulate formation, which is experienced as either beneficial or disadvantageous depending on the specific application. Moreover, with the recent introduction of Extreme Ultraviolet lithography to the field, semiconductor manufacturers are heavily investing in developing strategies to control contamination<sup>16,17</sup>, for which the only feasible way forward appears to be based on plasma technology, involving Coulomb interaction between the generated discharges and plasma-charged contaminants.

A crucial part of our understanding of cosmic and terrestrial complex and dusty plasmas lies in the complex yet elementary interaction between dust grains and the plasma environment in which they are embedded. Elementary interactions in a low-temperature plasma are by default dictated by free electrons, while the temperature of heavy species (ions and neutrals) remains close to room temperature. The low-energy part of the electron cloud determines the mean electron energy, the plasma conductivity, the Debye length and the ion sound speed in plasmas<sup>18</sup>. On the other hand, the high-energy part governs inelastic collision rates and the sheath potential<sup>18</sup>, of which the latter dictates the ion energy distribution and ion flux toward plasma-facing surfaces<sup>19</sup>. Hence, from a fundamental perspective, the electrons dictate fundamental processes, such as ionization and dissociation of plasma species, the creation and shielding of local electric fields, and the electrical charging of dust grains.

In particular, the process of plasma-based charging of nano- to micrometer-sized dust grains—along with its correlation with elementary electron dynamics—is crucial to understand with respect to all aforementioned research fields and applications. The field, in general, assumes that the electron plasma frequency greatly exceeds the electron-neutral momentum transfer collision frequency at low-pressure (typically, 500 MHz and 50 MHz, respectively, for pristine argon plasmas at 0.1 mbar (i.e., 75 mTorr)), and therefore the electron-neutral (momentum transfer) collision frequency has been neglected when developing theoretical frameworks for plasma-dust charging. This assumption applies to the orbital-motion-limited (OML) theory, introduced by Irving Langmuir<sup>20</sup>, which is the widely accepted theoretical framework for predicting the surface charge of dust grains in dusty plasmas.

In this work, we provide experimental evidence (see Fig. 1) that the electron-neutral collision frequency should be included in the dust charging theory by showing its dominance over other timescales in a dusty plasma. For this purpose, we measured—in addition to the electron plasma frequency  $f_{pe}$  (via the free electron density  $n_e$ ) which is widely used in literature to indicate and

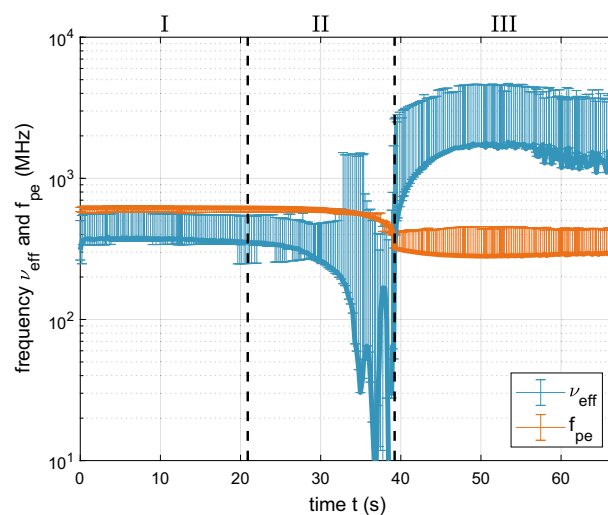


**Fig. 1 Characteristic frequencies of the plasma during dust grain**

**formation.** The effective collision frequency  $\nu_{\text{eff}}$  (blue line and error bars) and electron plasma frequency  $f_{pe}$  (orange line and error bars) are obtained from Microwave Cavity Resonance Spectroscopy measurements as a function of time, with respect to the moment of plasma initiation at  $t = 0$  s, during dust formation in a low-pressure radio-frequency driven capacitively-coupled argon-hexamethyldisiloxane (i.e., HMDSO) discharge. The error bars represent the effect of the (estimated) error in the determination of the resonance frequency and quality factor on the effective collision frequency and electron plasma frequency. The derivation of the error propagation is described in the subsection Microwave Cavity Resonance Spectroscopy in the Methods. The gas discharge was created under the following experimental conditions: partial argon pressure at  $5.7 \times 10^{-2}$  mbar (43 mTorr), partial HMDSO pressure at  $1.4 \times 10^{-2}$  mbar (11 mTorr), plasma volume of  $42 \text{ cm}^3$  ( $2.56 \text{ in}^3$ ), and absorbed power density of  $0.7 \text{ W cm}^{-3}$  ( $11.7 \text{ W in}^{-3}$ ).

monitor dust grain formation processes in plasmas—the electron-neutral collision frequency for momentum transfer (effective collision frequency  $\nu_{\text{eff}}$ ). To achieve this, an exemplary case of dust grain formation was studied in a low-pressure hexamethyldisiloxane (HMDSO) containing plasma (see the subsection “Experiment” and Fig. 2 in the Methods) by application of Microwave Cavity Resonance Spectroscopy (abbreviated to MCRS; see the subsection “Microwave Cavity Resonance Spectroscopy” in the Methods). This diagnostic method is based on detecting the amount of detuning of a resonant mode of a plasma-filled microwave cavity. The resonant mode is characterized by its spectral response, and a typical cavity response to the dusty plasma is shown in Fig. 3 in the subsection “Microwave Cavity Resonance Spectroscopy” in the Methods. The growth behavior of dust grains as typically occurs in terrestrial dusty plasmas is observed. However, our results also show that the effective collision frequency exceeds the electron plasma frequency when dust grains are formed. Moreover, at the approximate moment that particle agglomeration sets in, a peculiar nonmonotonous trend is observed in the electron collision frequency which has not been observed in prior studies. Hence, it is shown that the electron population is heavily affected by the formation of dust grains in addition to the well-established effect of electron depletion by dust grain charging<sup>21–23</sup>. This insight into the binary interaction between electrons and dust grains is of major importance for the earlier mentioned research fields and applications, and arguments that the effect should be incorporated in the existing paradigm and overall theoretical framework.

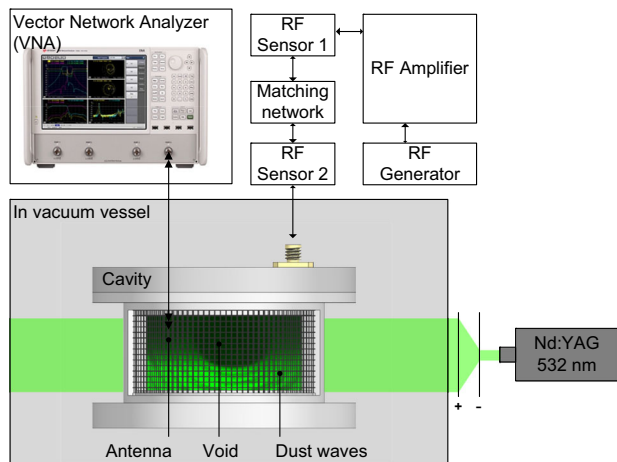


**Fig. 2 A schematic overview of the experimental setup.** The microwave cavity confined the argon-hexamethylidisiloxane discharge used for growing dust grains in vacuum, where the grey box defines the elements that were located inside the vacuum. The RF system supplied electrical power to the discharge, where the RF generator and amplifier provided continuous power to the matching network which ensured optimal power transfer to the plasma. The RF power was measured using power sensors. Meanwhile, the plasma response was monitored by the Vector Network Analyzer, and the dust grains were observed by capturing scattered laser light on a high-speed camera. The green laser beam (continuous power, Nd:YAG, wavelength 532 nm) was expanded in the axial direction of the cavity by two cylindrical lenses, which allowed the creation of a laser sheet (indicated by bright green area) that entered and left the cavity through two slits in the cavity's side walls.

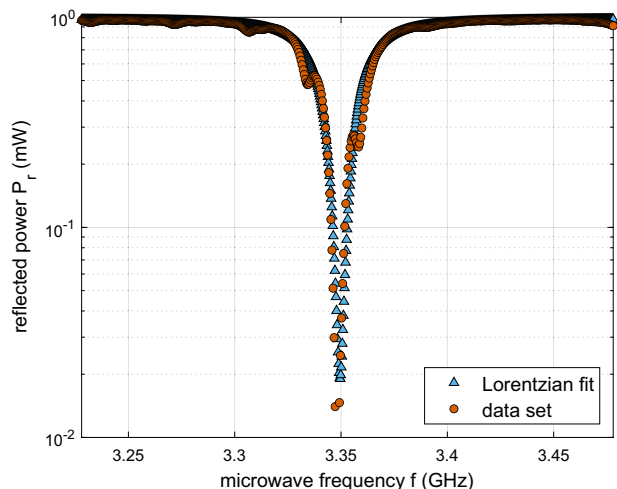


**Fig. 3 Typical microwave cavity response to dusty plasma.** The spectral response of the microwave cavity is depicted in terms of reflected power  $P_r$  as a function of microwave frequency  $f$ , and corresponding Lorentzian fit, at  $t = 32.8$  s. The Lorentzian fit is defined by the resonance frequency, at which the reflected power is minimal, and the quality factor which is related to the full-width-at-half-maximum of the Lorentzian curve.

## Results

**Dust formation process.** The process of dust formation in low-pressure reactive plasmas—typically taking between 1 and 100 seconds depending on the plasma conditions—is widely recognized due to numerous exemplary studies conducted on discharges in acetylene<sup>24,25</sup>, silane<sup>26</sup>, hexamethylidisiloxane<sup>27,28</sup>, methane<sup>29</sup>, and fluorocarbon<sup>30</sup>. In agreement with these studies, our temporally-resolved experiments obtaining the electron

plasma frequency for an exemplary low-pressure argon-hexamethylidisiloxane plasma—as shown in Fig. 1—indicate that the dust formation process chronologically follows three well-known phases: (I) nucleation, (II) agglomeration, and (III) accretion.

**Electron plasma frequency.** In phase I, the electron density—and therefore, the electron plasma frequency  $f_{pe}$ —remains nearly constant during the formation of nanometer-sized solid proto-particles (also termed primary clusters or nuclei). It can be seen from Fig. 1 that the (phase I-averaged) electron plasma frequency is 619 ( $-44/+12$ ) MHz (i.e.,  $n_e = 4 \times 10^9$  ( $-3.45 \times 10^9/+4.16 \times 10^9$ )  $\text{cm}^{-3}$ ), which is typical for low-temperature discharges during the nucleation of dust grains<sup>31,32</sup>.

In phase II, the electron plasma frequency first decreases gradually, after which it starts to decrease more rapidly toward the end of this phase ( $t \gtrsim 35$  s). This finding is also in agreement with the existing paradigm that the formation of clusters induces an additional electron loss channel due to electron attachment to the clusters, which lowers the overall electron density in the plasma<sup>33</sup>.

In phase III, the electron plasma frequency during the accretion phase is characterized by a low (phase III-averaged) value of 290 ( $-0/+150$ ) MHz. Comparing this value to the first phase, a threefold decrease of the electron plasma frequency means that the global electron density is nine times lower as these two quantities scale as  $f_{pe} \propto \sqrt{n_e}$ . Clearly, the effect of the permanent charging of the dust grains is visible, but the further growth of the dust grains does not significantly affect the absolute value of the electron plasma frequency throughout this third phase. While the dust grains grow in size and hence draw an increasing electron current from the discharge ( $I_e \propto a^2$ ), this additional electron loss is balanced by an increased ionization rate through a surge of the mean electron energy. Meanwhile, the electron density remains constant as can be seen from Fig. 1.

The measurement of the electron plasma frequency (i.e., the global electron density) agrees well with experiments described in the literature and the existing theoretical framework. However, measurement of the effective collision frequency in a plasma-nanoparticle system has not been reported in the literature before, although its measurement facilitates a direct comparison to the electron plasma frequency and provides insight into peculiarities.

**Effective collision frequency.** Here, we report a time-resolved trace of this effective collision frequency throughout the three earlier mentioned phases, revealing insight regarding the importance of elastic electron collisions in dusty plasmas.

In phase I, the effective collision frequency remains nearly constant at a (phase I-averaged) value of 368 ( $-30/+207$ ) MHz. As can be seen from Fig. 1, this value is below that of  $f_{pe}$ , and as generally accepted by the field, the electron dynamics of low-energy electrons remain collisionless during this phase.

In phase II, the effective collision frequency remains relatively constant at first (within error bounds), whereas the results mainly show significant changes in the effective collision frequency during the final part of this phase. In particular, towards the end of the coagulation phase, the effective collision frequency decreases to values below that of the first phase, while the decline of the global electron density is much smaller and occurs only during the final seconds of this phase. It should be noted that fluctuations of the effective collision frequency are a consequence of the measurement technique, because the quality factor approaches the pre-plasma value resulting in small values of  $\Delta(1/Q)$  (see the subsection “Microwave Cavity Resonance Spectroscopy” in the Methods). The decrease of the effective collision frequency may be explained by the clustering of

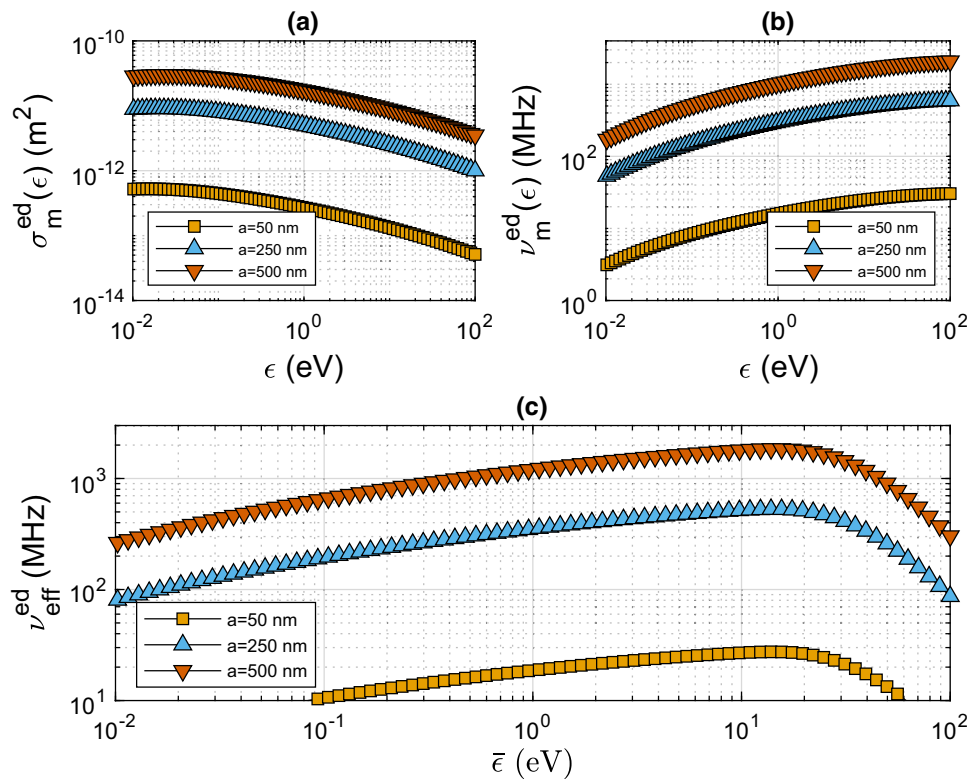


**Fig. 4** Theoretical evaluation of electron-dust momentum transfer collisions for different dust radii. **a** The momentum transfer cross section  $\sigma_m^{\text{ed}}$  is calculated using Eq. (15) as a function of electron energy  $\epsilon$ . **b** The momentum transfer collision frequency  $\nu_m^{\text{ed}}$  follows from the electron-dust momentum transfer cross section in combination with Eq. (14) as a function of the electron energy  $\epsilon$ . **c** The effective collision frequency  $\nu_{\text{eff}}^{\text{ed}}$  for electron-dust collisions is evaluated using Eq. (13), which is evaluated as a function of the mean electron energy  $\bar{\epsilon}$ . In each panel, the calculation of  $\sigma_m^{\text{ed}}$ ,  $\nu_m^{\text{ed}}$ , and  $\nu_{\text{eff}}^{\text{ed}}$  is performed for dust radii  $a = 50$  nm (orange squares),  $a = 250$  nm (blue upward-facing triangles), and  $a = 500$  nm (red downward-facing triangles), for a fixed dust density  $n_d = 10^8 \text{ cm}^{-3}$ .

(prototypical) nanoparticles for which the physical interpretation and the relation with the observed phenomenon is treated in the discussion section.

In phase III, the accretion phase is characterized by a surprisingly high (phase III-averaged) effective collision frequency of 1429 (−0/+2601) MHz, which exceeds the electron plasma frequency of 323 (−0/+176) MHz by almost a factor of five. Despite the predictive capability of the existing paradigm (see the subsection “Theoretical analysis” in the Methods), such values for the effective collision frequency were not stated or measured as of yet and appear crucial to account for in the orbital-motion-limited theoretical framework describing dust grain formation and growth in plasmas, even at low-pressure.

## Discussion

The time evolution of the electron plasma frequency serves as a benchmark for the identification of the different phases (i.e. nucleation, agglomeration, and accretion) in the overall dust grain growth process inside the plasma. During the first stage of nucleation, the electron plasma frequency is 575–631 MHz (resulting from  $n_e \sim 10^9\text{--}10^{10} \text{ cm}^{-3}$ ), which is typical for discharges driven by a radio-frequency voltage signal<sup>31,32</sup> or by a direct current<sup>34</sup>. Hereafter, the electron plasma frequency falls off by a factor of three decrease throughout the coagulation phase, which is in close agreement with experiments performed by other workers in the field<sup>35,36</sup>. As described in the literature, this trend is attributed to the permanent binding of electrons to dust grains.

During the second phase, i.e., the agglomeration phase, the effective collision frequency initially remains approximately

constant. This finding agrees with measurements performed by other workers<sup>24,37</sup>, and it relates to the plasma and dust properties. Despite the possible formation of small clusters in this phase, the electron-dust momentum transfer cross section is still irrelevant with respect to the (elastic) electron-neutral collisions in both the first and second part of this phase (for dust grain radii  $a \leq 50$  nm and dust density  $n_d \leq 10^8 \text{ cm}^{-3}$ , see Fig. 4 in the subsection “Theoretical analysis” in the Methods). The irrelevance of the electron-dust cross section for momentum transfer implies that the electron loss channel due to attachment of electrons to dust grains is also insignificant up to this point, and this implication is reflected by the stability of the electron plasma frequency and effective collision frequency.

At the end of the agglomeration phase, the effective collision frequency reaches minimum values  $\sim 10\text{--}100$  MHz. A possible explanation for the low effective collision frequency is the attachment of high-energy electrons to the agglomerating dust grains. As a result of the growth of dust grains due to the agglomeration of clusters that were formed during the first phase, the surface charge averaged over all protoparticles becomes increasingly negative when time progresses toward the end of the coagulation phase. The high-energy electrons collide most frequently with the dust grains because they travel larger distances than their slower counterparts within the same time frame. Consequently, the high-energy tail of the electron energy distribution is depleted, which results in an effective decrease of the mean electron energy on timescales related to the absorption of electrons by the small protoparticles.

The observed temporal decay of the effective collision frequency compares well with the absorption timescale governed by

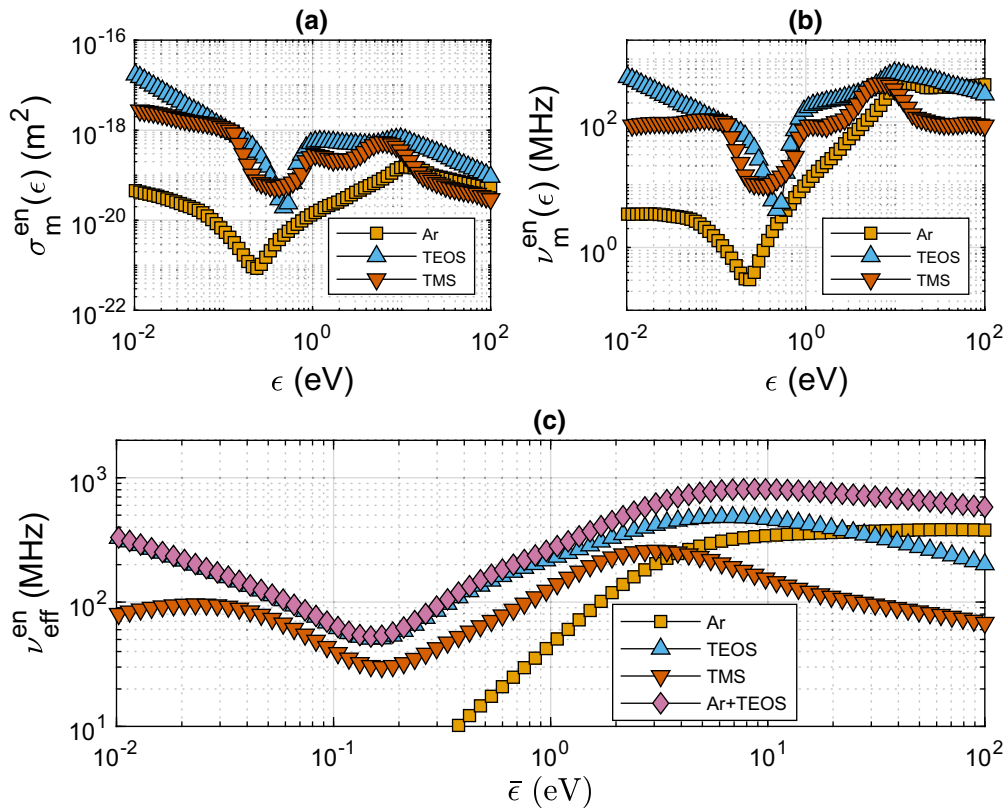


**Fig. 5 Theoretical evaluation of electron-neutral momentum transfer collisions for different neutral gas species.** The neutral gas species are denoted in the legend as argon (Ar, orange squares), tetraethylorthosilicate (TEOS, blue upward-facing triangles), and tetramethylsilane (TMS, red downward-facing triangles). **a** The momentum transfer cross section  $\sigma_m^{\text{en}}$  is obtained from literature for argon<sup>69</sup>, TEOS<sup>70,71</sup>, and TMS<sup>70,72,73</sup> as a function of electron energy  $\epsilon$ . **b** The momentum transfer collision frequency  $\nu_m^{\text{en}}$  is calculated using Eq. (14) as a function of electron energy  $\epsilon$ , using the neutral gas density  $n = 1.75 \times 10^{21} \text{ m}^{-3}$  (for pressure  $p = 7.1 \times 10^{-2} \text{ mbar}$ ) and the momentum transfer cross section. **c** The effective collision frequency  $\nu_{\text{eff}}^{\text{en}}$  is calculated using Eq. (13) as a function of the electron mean energy  $\bar{\epsilon}$ . The total effective collision frequency (Ar+TEOS, purple diamonds) was calculated using the argon and TEOS values weighted by the partial argon pressure  $p_{\text{Ar}} = 5.4 \times 10^{-2} \text{ mbar}$  and partial TEOS pressure  $p_{\text{TEOS}} = 1.7 \times 10^{-2} \text{ mbar}$ , where the latter was defined equal to the partial hexamethyldisiloxane (HMDSO) pressure during the experiment.

the electron and ion currents<sup>38</sup>:

$$\tau_A \approx \left( \pi a^2 n_d \bar{v}_i \left( 1 + \frac{\phi_d}{T_i} \right) \right)^{-1} \approx 0.65 \text{ s}, \quad (1)$$

where  $a$  and  $n_d$  denote the dust grain radius and number density,  $\bar{v}_i$  the ion thermal velocity,  $\phi_d$  the dust floating potential, and  $T_i$  the ion temperature, respectively. For this calculation, dust radius and density are  $a = 1 \text{ nm}$  and  $n_d = 10^8 \text{ cm}^{-3}$ , dust floating potential<sup>38</sup>  $\phi_d = -eq_d / (4\pi\epsilon_0 a) \approx -1.44 \text{ V}$  (with dust charge  $q_d = 1$ <sup>39</sup>, elementary charge  $e$ , and vacuum permittivity  $\epsilon_0$ ), and ion temperature  $T_i = 0.026 \text{ eV}$  (i.e., 300 K). The effective collision frequency must follow this behavior, because the electron-dust momentum transfer cross section is much smaller than the electron-neutral momentum transfer cross section.

The steep increase of the effective collision frequency at the end of this phase shows that the depletion of electrons is terminated as they are repelled by the permanent negative surface potential of the formed and growing dust grains. In addition, further supporting the latter explanation, the electron plasma frequency suddenly decreases at the end of the coagulation phase due to this permanent charging of the dust grains, and this means that the energy input per electron increases as the (RF) electric field remains unchanged. The jump in the effective collision frequency can potentially be attributed to the effect of increasing electron mean energy on the electron-neutral momentum transfer cross

section. From a theoretical investigation (see Fig. 4 in the subsection “Theoretical analysis” in the Methods), it can be concluded that the electron-dust contribution is at most 24 MHz for  $a = 50 \text{ nm}$  (assumed upper limit of the average dust radius just after coagulation<sup>40,41</sup>). By contrast, the electron-neutral contribution ranges from 100 MHz to 400 MHz, for the mean electron energy  $\epsilon = 0.3\text{--}1.7 \text{ eV}$ , respectively (as can be seen from Fig. 5 in the subsection “Theoretical analysis” in the Methods). This implies that the electron means energy is low before coagulation, and afterwards rapidly increases to higher values during the third phase.

During the third phase, i.e., the accretion phase, the presence of dust grains has a large impact on the electron dynamics via the effect of the electron mean energy on the electron-neutral (momentum transfer) collisions. In this phase, dust grain radii and number densities are typically in the range of 50–250 nm and  $\sim 10^8 \text{ cm}^{-3}$  in the discharge center<sup>41–43</sup>. This means that the contribution of electron-dust momentum transfer collisions to  $\nu_{\text{eff}}$  is about 20–440 MHz for  $\epsilon \sim 1\text{--}3 \text{ eV}$  and  $a = 50\text{--}250 \text{ nm}$  (see Fig. 4 in the subsection “Theoretical analysis” in the Methods). Although the electron-dust contribution is non-negligible according to the theory, the electron-neutral contribution to the effective collision frequency remains dominant. It is well-known that the dust grain potential, mean electron energy, electron energy distribution, relevant collision partners, and corresponding cross sections change simultaneously during the

third stage. Clearly, the effective collision frequency is governed by this complex interplay between the plasma and dust grains.

The main experimental finding of the presented work is the fact that, in a dust-forming low-pressure plasma, the effective electron collision frequency may become considerably higher than the electron plasma frequency. The implications of this finding are related to the most commonly used theory throughout the field to predict dust grain charging in low-temperature, low-pressure plasmas: the orbital-motion-limited (OML) theory. There are three essential principles underlying the OML theory, of which we consider the first one: electrons and ions experience collisionless orbits in the electrostatic (Debye) vicinity of a dust grain immersed in a quasi-neutral plasma environment<sup>44</sup>. In plasma physical terms, this means that the following ordering of dust and plasma parameters must apply:  $a \ll \lambda_D \ll l$ , where  $\lambda_D$  is the Debye length and  $l$  the mean free path of the species under consideration. In other words, the Debye sphere virtually enclosing the dust grain is much larger than the grain itself, and collisions do not occur within the Debye sphere. Considering the electrons, the assumption that the electron mean free path is much larger than the electron Debye length means that the electron current towards the dust grain is collisionless.

Serious effort has been put into the extension, modelling, and verification of the OML theory<sup>44–49</sup>. For example, under certain conditions of pressure and dust grain size, there is a large probability that ions experience on average one collision with a neutral gas particle during their travel across the Debye sphere enclosing the dust grain<sup>50–52</sup>. In the hydrodynamic limit, ion-neutral collisions are so frequent that the ion dynamics can be described as a continuum<sup>53</sup>. Yet, in all such cases, the electron current has been considered collisionless until now. However, our results show that the electron current during the third phase—when permanently charged dust grains are in fact present in large quantities—resides in a similar situation as the ion current in the weakly collisional regime. This is because the electron mean free path is only  $l_e = \bar{v}_e / \nu_{\text{eff}} = 364 \mu\text{m}$ , while the electron Debye length is  $\lambda_{De} = \bar{v}_e / f_{pe} = 2127 \mu\text{m}$ , given that  $\bar{v}_e$  is the electron thermal velocity assuming  $T_e = 1 \text{ eV}$ . This implies that the electron current is collisional as  $l_e \ll \lambda_{De}$  and that the expression for the electron current in the overall plasma-dust charging framework (e.g., the OML theory) should incorporate electron-neutral (momentum transfer) collisions occurring within the Debye sphere enclosing the dust grain. As a matter of fact, the elastic electron collisions suppress the ability of the electrons to shield perturbations, and therefore the Debye length will be larger for the same electron density in case of a significant effective collision frequency.

The relevance of the effective collision frequency also affects other fundamental processes in the plasma such as electron heating. The dusty plasma (probed during the accretion phase) operates in the so-called  $\Omega$ -mode or drift-ambipolar mode<sup>54–58</sup>, where a drift electric field accelerates electrons in the plasma bulk and an ambipolar field—created by electron density gradients—heats electrons near the sheath edge. The drift electric field is induced by the low bulk electrical conductivity due to electron depletion, which is similar to the effect of a high electron-neutral collision frequency in atmospheric pressure discharges<sup>59,60</sup>. In addition to previous findings on electron depletion for  $\Omega$ -mode operation, the significance of the effective collision frequency in our low-pressure plasma experiment suggests that the electrical conductivity is further reduced. Consequently, this implies that the drift electric field results in stronger electron heating compared to plasma conditions with insignificant effective collision frequency.

## Conclusion

We have shown that the electron current towards a dust grain can be collisional during the accretion phase of a low-pressure dusty plasma—which holds for  $t \geq 39 \text{ s}$  in our measurements—in contrast to the existing paradigm. This conclusion is based on our measurements showing that the effective collision frequency exceeds the electron plasma frequency multiple times during the third phase of dust growth in a typical low-pressure discharge. This translates into an electron mean free path smaller than the electron Debye length, meaning that the electrons in the dust grain sheath collide elastically multiple times before they complete their orbit. It is exactly this assumption of a collisionless electron current that forms an integral part of the widely accepted orbital-motion-limited theory in which electron-neutral collisions have always been neglected, up to now. We expect that this result is also relevant for other plasmas in which dust grains are embedded, and that electron-neutral momentum transfer collisions become even more dominant in cases of higher gas pressure, lower electron density, and larger dust grain size.

## Methods

**Experiment.** The dust grains were grown in a gas discharge at room temperature produced in a vacuum vessel with controlled in- and outlet of neutral gas at a reduced pressure. The vessel had a diameter of 60 cm (23.6 in) and a height of 45 cm (17.7 in), and it contained a cylindrical cavity with an inner diameter of  $D_c = 6.6 \text{ cm}$  (2.6 in) and an inner height of  $H_c = 4.0 \text{ cm}$  (1.6 in). In this cavity, discharge electrodes were integrated to produce and confine the plasma. Vertical slits in the cylindrical wall allowed the laser beam to enter and exit the cavity, whereas a stainless steel mesh allowed scattered light to be observed by a camera. Meanwhile, the slits and mesh also allowed the gas to freely diffuse in and out of the cavity. Widely used in plasma processing, hexamethyldisiloxane (HMDSO, CAS Registry Number: 107-46-0, purity  $\geq 99.5\%$ ) was introduced through evaporation from a liquid-containing volume connected to the vessel, while argon (purity  $\geq 99.999\%$ ) was introduced using a mass flow controller. An operating pressure of  $7.1 \times 10^{-2} \text{ mbar}$  (53 mTorr) was installed by balancing the inflow of the vapor-gas mixture by an outflow of gas species using a turbo-molecular and dry scroll pump in series (base pressure  $\sim 10^{-7} \text{ mbar}$  ( $7.5 \times 10^{-5} \text{ mTorr}$ ) without inflow), which also were continuously running during the experiment to maintain a high purity level. Electrical power was capacitively coupled into the neutral gas mixture inside the plasma-confining cavity by applying an alternating voltage to the (electrically isolated) top electrode, at a (radio-)frequency of 13.56 MHz, which is common for low-pressure discharges. The alternating voltage was generated using an RF signal generator combined with an amplifier. To optimize the transfer of electrical power, a matching network was used to adjust the total electrical impedance (impedance of the discharge cavity plus that of the matching network) observed by the RF amplifier to that of the amplifier output circuit, i.e., 50  $\Omega$ . As a consequence, a strong electric field alternating at radio-frequency (RF) induced a gas discharge sustained at room temperature and subsequently induced the chemical reactions necessary for the polymerization, clustering, and agglomeration of molecular clusters, eventually resulting in (nanometer-sized) dust grains.

**Microwave Cavity Resonance Spectroscopy.** The gas discharge was produced inside a microwave cavity to enable Microwave Cavity Resonance Spectroscopy experiments, as depicted in Fig. 2. A commercial network analyzer (E5072A, Keysight Technologies) was used to probe the spectral response of the fundamental mode TM<sub>010</sub> by measuring the amount of reflected microwave power over a fixed microwave frequency range. The presence of free electrons created by the gas discharge de-tuned the resonant mode such that the corresponding resonance frequency and quality factor were shifted with respect to the case without plasma. At a sample rate of  $\sim 6 \text{ Hz}$ , the network analyzer obtained spectral responses during the process of the formation of dust grains.

Microwave Cavity Resonance Spectroscopy (MCRS) relies on the difference in (complex) permittivity between a gas discharge compared to vacuum:

$$\Delta \tilde{\epsilon} = \tilde{\epsilon}_1 - \epsilon_0, \quad (2)$$

where  $\tilde{\epsilon}_1$  denotes the (complex) plasma permittivity, and  $\epsilon_0$  the vacuum permittivity. The (complex) plasma permittivity depends on the electron plasma frequency and on the effective collision frequency (due to elastic electron collisions with neutrals and dust) as<sup>61</sup>:

$$\tilde{\epsilon}_1 = \epsilon_0 \left( 1 - \frac{(2\pi f_{pe})^2}{\nu_{\text{eff}}^2 + (2\pi f)^2} - i \frac{\nu_{\text{eff}}}{2\pi f} \frac{(2\pi f_{pe})^2}{\nu_{\text{eff}}^2 + (2\pi f)^2} \right), \quad (3)$$

with the electron plasma frequency  $f_{pe}$ , the effective collision frequency  $\nu_{\text{eff}}$ , the microwave frequency  $f$ , and  $i$  the imaginary number. The relation between the

electron plasma frequency and the free electron density reads:

$$f_{pe} = \frac{1}{2\pi} \sqrt{\frac{n_e e^2}{\epsilon_0 m_e}}, \quad (4)$$

with  $n_e$  the free electron density,  $e$  the elementary charge, and  $m_e$  the electron mass.

The change in permittivity is directly related to changes in the free electron density and in the effective collision frequency, which de-tune the characteristics of the cavity's resonant modes. A resonant mode is characterized by the spectral position of the resonance frequency  $f_{res}$  and the quality factor  $Q_{res}$  (related to the full-width-at-half-maximum of a resonance peak), which relate to changes in the (complex) permittivity  $\Delta\tilde{\epsilon}$  of the medium contained inside the microwave cavity according to the Slater perturbation theorem as<sup>62–64</sup>:

$$\frac{\Delta f}{f_0} + i \frac{1}{2} \Delta \left( \frac{1}{Q} \right) = - \frac{\int \int \int_{V_c} \Delta\tilde{\epsilon} |\mathbf{E}|^2 d\mathbf{r}}{2\epsilon_0 \int \int \int_{V_c} |\mathbf{E}|^2 d\mathbf{r}}. \quad (5)$$

Here,  $\Delta f = f_1 - f_0$  denotes the plasma-induced shift in resonance frequency,  $f_1$  the resonance frequency with plasma,  $f_0$  the resonance frequency without plasma,  $\mathbf{E}$  the (local) microwave electric field inside the cavity,  $V_p$  the plasma volume,  $V_c$  the cavity volume, and  $\mathbf{r}$  the spatial coordinate vector.

The electric-field-weighted volume ratio is often defined to express the ratio between the plasma volume  $V_p$  (i.e. the perturbed volume of the cavity) and the cavity volume:

$$\mathcal{V} = \frac{\int \int \int_{V_p} |\mathbf{E}|^2 d\mathbf{r}}{\int \int \int_{V_c} |\mathbf{E}|^2 d\mathbf{r}}. \quad (6)$$

This definition is allowed upon assuming that the perturbation homogeneously disturbs the resonant mode, and hence, the complex permittivity can be taken out of the integral in Equation (5). Consequently, the effective collision frequency and electron plasma frequency can be derived by combining Equation (5) with Equations (2)–(3) such that:

$$\nu_{eff} = \pi f_1^2 \frac{\Delta(1/Q)}{\Delta f}, \quad (7)$$

and

$$f_{pe} = \sqrt{\frac{2f_1 \Delta f}{\mathcal{V}}}. \quad (8)$$

As can be seen, the volume ratio does not affect the effective collision frequency, but enters the electron plasma frequency evaluation. The electric-field-weighted volume ratio was estimated equal to 0.54 using  $V_p = \pi/4 D_p^2 H_p$  and  $V_c = \pi/4 D_c^2 H_c$ , with the plasma diameter  $D_p = 5.6$  cm, and plasma height  $H_p = 3.0$  cm (where a sheath size of 0.5 cm was assumed). This estimate for  $\mathcal{V}$  was included in the upper bound for  $f_{pe}$ .

A Vector Network Analyzer was used to obtain the spectral response over the microwave frequency range  $f = 3.228$ – $3.478$  GHz, which includes the resonant peak of the empty cavity and that of the plasma-filled cavity. The plasma-induced shifts of the resonance frequency were in the order of  $\sim 100$  MHz. A Lorentzian curve fit through the data around the resonant peak was then applied to obtain the resonance frequency and the quality factor. This fit curve was defined as:

$$P_r = A \frac{\left( \frac{f_{res}}{2Q_{res}} \right)^2}{(f - f_{res})^2 + \left( \frac{f_{res}}{2Q_{res}} \right)^2} + a_0 + a_1 (f - f_{res}), \quad (9)$$

where  $A$ ,  $a_0$ , and  $a_1$  are scaling factors for the Lorentzian curve and linear offsets in the microwave system, and  $f_{res}$  and  $Q_{res}$  are the resonance frequency and quality factor. Figure 3 provides a typical spectral response of the plasma-filled cavity at a certain time. This microwave spectrum contains a ( $TM_{010}$ ) resonant peak and some local resonances due to cabling and feedthroughs. The spectral position and shape of these “background” resonances were verified to be static and independent of the varying spectral position and shape of the resonant peak. The abovementioned Lorentzian fit was applied to the data set, where data points corresponding to the local minima were excluded from the fitting procedure to produce the nominal values for  $f_{pe}$  and  $\nu_{eff}$ . To determine the upper limit of the measurement errors  $\Delta f_0$ ,  $\Delta f_1$ ,  $\Delta Q_0$  and  $\Delta Q_1$ , the complete data set (including the spectrally localized background resonances) was used.

The error propagation from  $f_{res}$  and  $Q_{res}$  to  $f_{pe}$  and  $\nu_{eff}$  was established by applying linear perturbation analysis to Equations (7) and (8). Performing the algebra results in the desired expression for the error in  $\nu_{eff}$  as a function of the perturbed measurement variables:

$$\begin{aligned} \Delta \nu_{eff} = & \left( \pi f_1^2 \frac{\Delta(1/Q)}{\Delta f^2} \right) \Delta f_0 + \left( \frac{\pi f_1^2}{\Delta f} \frac{1}{Q_0^2} \right) \Delta Q_0 \\ & + \left( 2\pi f_1 \frac{\Delta(1/Q)}{\Delta f} - \pi f_1^2 \frac{\Delta(1/Q)}{\Delta f^2} \right) \Delta f_1 \\ & - \left( \frac{\pi f_1^2}{\Delta f} \frac{1}{Q_1^2} \right) \Delta Q_1. \end{aligned} \quad (10)$$

A similar exercise applied to Equation (8) results in the error propagation for  $f_{pe}$ :

$$\begin{aligned} \Delta f_{pe} = & \frac{1}{2} \left( \frac{(2\pi f_1)^2 + \nu_{eff}^2}{2\mathcal{V}} \frac{\Delta f}{f_1} \right)^{-3/2} \\ & \times \left\{ \left( \frac{(2\pi f_1)^2 + \nu_{eff}^2}{2\mathcal{V}} \frac{1}{f_1} \right) \Delta f_0 - \left( \frac{\pi f_1}{\mathcal{V}} \frac{1}{Q_0^2} \right) \Delta Q_0 \right. \\ & - \left( \frac{4\pi^2}{2\mathcal{V}} (2f_1 - f_0) + \frac{\nu_{eff}^2 f_0}{2\mathcal{V} f_1^2} \right) \Delta f_1 \\ & \left. + \left( \frac{\pi f_1}{\mathcal{V}} \frac{1}{Q_1^2} \right) \Delta Q_1 \right\}. \end{aligned} \quad (11)$$

**Theoretical analysis.** The total effective collision frequency of electrons with other species in dust grain-forming plasmas comprises the sum of effective collision frequencies due to electron-neutral and electron-dust collisions:

$$\nu_{eff} = \nu_{eff}^{en} + \nu_{eff}^{ed}. \quad (12)$$

Here, the electron-neutral collision frequency consists of the effective collision frequency due to multiple neutral gas species, such as argon, hexamethyldisiloxane, and possibly by-products. The effective collision frequency originates from the fact that the momentum transfer collision frequency  $\nu_m$  depends on the electron energy  $\epsilon$ <sup>65</sup>:

$$\nu_{eff} = \frac{\int_0^\infty \epsilon^{3/2} \frac{\nu_m(\epsilon)}{\nu_m^2(\epsilon) + \omega^2} \frac{dF}{d\epsilon} d\epsilon}{\int_0^\infty \epsilon^{3/2} \frac{1}{\nu_m^2(\epsilon) + \omega^2} \frac{dF}{d\epsilon} d\epsilon}, \quad (13)$$

with  $\omega = 2\pi f$  the (angular) microwave frequency and  $F$  the electron energy distribution function (EEDF). A Maxwellian EEDF is assumed with mean electron energy  $\bar{\epsilon}$ . The momentum transfer collision frequency follows by assuming a Lorentz gas such that

$$\nu_m = n\sigma_m \bar{v}_e, \quad (14)$$

which includes a fixed background of neutral gas or dust grains of density  $n$ , a momentum transfer cross section for electron-neutral or electron-dust collisions  $\sigma_m$ , and the electron thermal velocity  $\bar{v}_e$ .

The cross section and collision frequency for electron-dust momentum transfer, and the effective collision frequency for that process, are depicted in Fig. 4 (for a Maxwell-Boltzmann electron energy distribution). The cross section for electron-dust momentum transfer follows from the theory<sup>66,67</sup> and agrees well with the simulations by Choi and Kushner<sup>68</sup>. Fundamentally, the electron-dust interaction involves the electron scattering from charged dust grains and the attachment of electrons onto the surface. The elastic scattering of electrons due to the dust potential resembles the momentum transfer process, from which the electron-dust momentum transfer cross section can be derived<sup>67</sup>:

$$\sigma_m^{ed}(\epsilon) = \pi a^2 \left( -\frac{\phi_d}{\epsilon} \right)^2 \exp\left( \frac{2a}{\lambda_L} \right) \ln \Lambda, \quad (15)$$

with the dust surface potential  $\phi_d$ , the Coulomb parameter

$$\Lambda = -\frac{\lambda_L T_e}{a\phi_d}, \quad (16)$$

and  $\lambda_L$  as the linearized Debye length<sup>67</sup>.

Similarly, the electron-neutral momentum transfer frequency can be evaluated theoretically using Equations (13) and (14). Figure 5 depicts the electron-neutral momentum transfer cross section, momentum transfer collision frequency, and effective collision frequency using cross section data for argon<sup>69</sup>, tetraethylorthosilicate (TEOS)<sup>70,71</sup>, and tetramethylsilane (TMS)<sup>70,72,73</sup>. Although several HMDSO-related plasma processes have been studied<sup>74,75</sup>, cross section data for electron-HMDSO momentum transfer is unavailable in literature, and hence, the calculations with the aforementioned precursors are considered as most representative.

## Data availability

The measurement data is available from the corresponding author upon reasonable request.

## Code availability

The computer code used for the data analysis and interpretation is available from the corresponding author upon reasonable request.

Received: 3 May 2021; Accepted: 24 September 2021;

Published online: 22 October 2021

## References

1. Wickramasinghe, N. C. Small dust grains and the heating of HI clouds. *Nature* **227**, 587–588 (1970).

2. Merino, P. et al. Graphene etching on SiC grains as a path to interstellar polycyclic aromatic hydrocarbons formation. *Nat. Commun.* **5**, 3054 (2014).
3. Molster, F. J. et al. Low-temperature crystallization of silicate dust in circumstellar disks. *Nature* **401**, 563–565 (1999).
4. Yang, T. et al. Directed gas phase formation of silicon dioxide and implications for the formation of interstellar silicates. *Nat. Commun.* **9**, 774 (2018).
5. Vinković, D. Radiation-pressure mixing of large dust grains in protoplanetary disks. *Nature* **459**, 227–229 (2009).
6. Dulieu, F. et al. How micron-sized dust particles determine the chemistry of our Universe. *Sci. Rep.* **3**, 1338 (2013).
7. Nakano, H. et al. Precometary organic matter: a hidden reservoir of water inside the snow line. *Sci. Rep.* **10**, 7755 (2020).
8. Gall, C. et al. Rapid formation of large dust grains in the luminous supernova 2010jl. *Nature* **511**, 326–329 (2014).
9. Dunne, L., Eales, S., Ivison, R., Morgan, H. & Edmunds, M. Type II supernovae as a significant source of interstellar dust. *Nature* **424**, 285–287 (2003).
10. Tarafdar, S. & Wickramasinghe, N. Charged dust grains and excitation of rotational levels of interstellar molecular hydrogen. *Nature* **254**, 203–205 (1975).
11. Shukla, P. K. A survey of dusty plasma physics. *Phys. Plasmas* **8**, 1791 (2001).
12. Jana, M., Sen, A. & Kaw, P. Collective effects due to charge-fluctuation dynamics in a dusty plasma. *Phys. Rev. E* **48**, 3930–3933 (1993).
13. Van Minderhout, B. et al. Charge control of micro-particles in a shielded plasma afterglow. *Plasma Sources Sci. Technol.* **29**, 065005 (2020).
14. Lyon, M., Bergeson, S. D., Hart, G. & Murillo, M. S. Strongly-coupled plasmas formed from laser-heated solids. *Sci. Rep.* **5**, 1–7 (2015).
15. Maddox, J. Plasma dust as model crystals. *Nature* **370**, 411 (1994).
16. van de Kerkhof, M. A., Galutschek, E., Yakunin, A., Cats, S. & Cloin, C. Particulate and molecular contamination control in EUV-induced H<sub>2</sub>-plasma in EUV lithographic scanner. *Proc. SPIE* **11489**, 114890K (2020).
17. Beckers, J., van Minderhout, B., Blom, P., Kroesen, G. & Peijnenburg, T. Particle contamination control by application of plasma. *Proc. SPIE* **11323**, 113232L (2020).
18. Kolobov, V. & Godyak, V. Electron kinetics in low-temperature plasmas. *Phys. Plasmas* **26**, 060601 (2019).
19. Lieberman, M. A. & Lichtenberg, A. J. *Principles of Plasma Discharges and Materials Processing* (John Wiley & Sons Inc, 2005).
20. Langmuir, I. Oscillations in ionized gases. *Proc. Natl Acad. Sci. USA.* **14**, 627–637 (1928).
21. Sukhinin, G. I. & Fedoseev, A. V. Influence of dust-particle concentration on gas-discharge plasma. *Phys. Rev. E* **81**, 016402 (2010).
22. Douglass, A., Land, V., Matthews, L. & Hyde, T. Dust particle charge in plasma with ion flow and electron depletion near plasma boundaries. *Phys. Plasmas* **18**, 083706 (2011).
23. Goertz, I., Greiner, F. & Piel, A. Effects of charge depletion in dusty plasmas. *Phys. Plasmas* **18**, 013703 (2011).
24. Ussenov, Y. A., von Wahl, E., Marvi, Z., Ramazanov, T. S. & Kersten, H. Langmuir probe measurements in nanodust containing argon-acetylene plasmas. *Vacuum* **166**, 15–25 (2019).
25. Denysenko, I. B. et al. Plasma properties as function of time in Ar/C<sub>2</sub>H<sub>2</sub> dust-forming plasma. *J. Phys. D: Appl. Phys.* **53**, 135203 (2020).
26. Stoffels, W. W., Stoffels, E., Kroesen, G. M. & De Hoog, F. J. Electron density fluctuations in a dusty Ar/SiH<sub>4</sub> rf discharge. *J. Appl. Phys.* **78**, 4867–4872 (1995).
27. Garofano, V., Stafford, L., Despax, B., Clergereaux, R. & Makasheva, K. Cyclic evolution of the electron temperature and density in dusty low-pressure radio frequency plasmas with pulsed injection of hexamethyldisiloxane. *Appl. Phys. Lett.* **107**, 183104 (2015).
28. Despax, B., Makasheva, K. & Caqueneau, H. Cyclic powder formation during pulsed injection of hexamethyldisiloxane in an axially asymmetric radiofrequency argon discharge. *J. Appl. Phys.* **112**, 093302 (2012).
29. Beckers, J. & Kroesen, G. M. W. Gas temperature dependence of coagulation onset times for nanoparticles in low pressure hydrocarbon plasmas. *Appl. Phys. Lett.* **103**, 123106 (2013).
30. Haverlag, M., Kroesen, G. M., Bisschops, T. H. & de Hoog, F. J. Measurement of electron densities by a microwave cavity method in 13.56-MHz RF plasmas of Ar, CF<sub>4</sub>, C<sub>2</sub>F<sub>6</sub>, and CHF<sub>3</sub>. *Plasma Chem. Plasma Process.* **11**, 357–370 (1991).
31. Schlebrowski, T., Bahre, H., Böke, M. & Winter, J. Monitoring particle growth in deposition plasmas. *Plasma Sources Sci. Technol.* **22**, 065014 (2013).
32. Denysenko, I. B. et al. Modeling of argon-acetylene dusty plasma. *Plasma Phys. Controlled Fusion* **61**, 014014 (2019).
33. Bouchoule, A. *Dusty Plasmas* (John Wiley & Sons Inc, 1999).
34. Michau, A., Lombardi, G., Arnas, C., Bonnin, X. & Hassouni, K. Modeling of dust formation in a DC discharge. *J. Nucl. Mater.* **415**, S1077–S1080 (2011).
35. Berndt, J. et al. Some aspects of reactive complex plasmas. *Contributions Plasma Phys.* **49**, 107–133 (2009).
36. Stefanović, I., Kovačević, E., Berndt, J. & Winter, J. Non-equilibrium processes and dust formation in low pressure reactive plasmas. *J. Phys.: Conf. Ser.* **71**, 012015 (2007).
37. Beckers, J. *Dust Particle(s) (as) Diagnostics in Plasmas* (Eindhoven University of Technology, 2011).
38. Couëdel, L., Mikikian, M., Boufendi, L. & Samarian, A. A. Residual dust charges in discharge afterglow. *Phys. Rev. E* **74**, 026403 (2006).
39. Michau, A., Arnas, C., Lombardi, G., Bonnin, X. & Hassouni, K. Nanoparticle formation and dusty plasma effects in DC sputtering discharge with graphite cathode. *Plasma Sources Sci. Technol.* **25**, 015019 (2016).
40. Van De Wetering, F. M., Nijdam, S. & Beckers, J. Conclusive evidence of abrupt coagulation inside the void during cyclic nanoparticle formation in reactive plasma. *Appl. Phys. Lett.* **109**, 043105 (2016).
41. Bouchoule, A. & Boufendi, L. Particulate formation and dusty plasma behaviour in argon-silane RF discharge. *Plasma Sources Sci. Technol.* **2**, 204–213 (1993).
42. Boufendi, L. et al. Particle-particle interactions in dusty plasmas. *J. Appl. Phys.* **73**, 2160–2162 (1993).
43. Tadsen, B., Greiner, F., Groth, S. & Piel, A. Self-excited dust-acoustic waves in an electron-depleted nanodusty plasma. *Phys. Plasmas* **22**, 113701 (2015).
44. Tang, X. Z. & Delzanno, G. L. Orbital-motion-limited theory of dust charging and plasma response. *Phys. Plasmas* **21**, 123708 (2014).
45. Chahl, H. S. & Gopalakrishnan, R. High potential, near free molecular regime Coulombic collisions in aerosols and dusty plasmas. *Aerosol Sci. Technol.* **53**, 933–957 (2019).
46. Suresh, V., Li, L., Redmond Go Felipe, J. & Gopalakrishnan, R. Modeling nanoparticle charge distribution in the afterglow of non-thermal plasmas and comparison with measurements. *J. Phys. D: Appl. Phys.* **54**, 275205 (2021).
47. Allen, J. E., Annaratone, B. M. & de Angelis, U. On the orbital motion limited theory for a small body at floating potential in a Maxwellian plasma. *J. Plasma Phys.* **63**, 299–309 (2000).
48. Delzanno, G. L. & Tang, X. Z. Comparison of dust charging between orbital-motion-limited theory and particle-in-cell simulations. *Phys. Plasmas* **22**, 113703 (2015).
49. Scott, L., Ellis, N., Chen, M., Matthews, L. S. & Hyde, T. W. Mapping the Plasma Potential in a Glass Box. *IEEE Trans. Plasma Sci.* **47**, 3079–3086 (2019).
50. Khrapak, S. A. et al. Grain charge in the bulk of gas discharges. *AIP Conf. Proc.* **799**, 177–180 (2005).
51. Lampe, M., Gavrishchaka, V., Ganguli, G. & Joyce, G. Effect of trapped ions on shielding of a charged spherical object in a plasma. *Phys. Rev. Lett.* **86**, 5278–5281 (2001).
52. Hoppel, W. A. & Frick, G. M. Ion-aerosol attachment coefficients and the steady-state charge distribution on aerosols in a bipolar ion environment. *Aerosol Sci. Technol.* **5**, 1–21 (1986).
53. Gatti, M. & Kortshagen, U. Analytical model of particle charging in plasmas over a wide range of collisionality. *Phys. Rev. E* **78**, 046402 (2008).
54. Killer, C., Bandelow, G., Matyash, K., Schneider, R. & Melzer, A. Observation of  $\Omega$  mode electron heating in dusty argon radio frequency discharges. *Phys. Plasmas* **20**, 083704 (2013).
55. Schulze, J. et al. Ionization by drift and ambipolar electric fields in electronegative capacitive radio frequency plasmas. *Phys. Rev. Lett.* **107**, 275001 (2011).
56. Schulze, J., Donkó, Z., Derzsi, A., Korolov, I. & Schuengel, E. The effect of ambipolar electric fields on the electron heating in capacitive RF plasmas. *Plasma Sources Sci. Technol.* **24**, 015019 (2015).
57. Schüngel, E., Mohr, S., Iwashita, S., Schulze, J. & Czarnetzki, U. The effect of dust on electron heating and dc self-bias in hydrogen diluted silane discharges. *J. Phys. D: Appl. Phys.* **46**, 175205 (2013).
58. Boeuf, J. P. & Belenger, P. Transition from a capacitive to a resistive regime in a silane radio frequency discharge and its possible relation to powder formation. *J. Appl. Phys.* **71**, 4751–4754 (1992).
59. Hemke, T. et al. Ionization by bulk heating of electrons in capacitive radio frequency atmospheric pressure microplasmas. *Plasma Sources Sci. Technol.* **22**, 015012 (2013).
60. Liu, D. W., Iza, F. & Kong, M. G. Electron heating in radio-frequency capacitively coupled atmospheric-pressure plasmas. *Appl. Phys. Lett.* **93**, 261503 (2008).
61. van der Schans, M. et al. Decay of the electron density and the electron collision frequency between successive discharges of a pulsed plasma jet in N<sub>2</sub>. *Plasma Sources Sci. Technol.* **28**, 035020 (2019).
62. Slater, J. C. Microwave Electronics. *Rev. Mod. Phys.* **18**, 441–512 (1946).
63. Biondi, M. A. Measurement of the electron density in ionized gases by microwave techniques. *Rev. Sci. Instrum.* **22**, 500–502 (1951).
64. Harrington, R. F. *Time-Harmonic Electromagnetic Fields*. (Wiley-IEEE Press, New York, 2001).
65. McColl, W., Brooks, C. & Brake, M. L. Electron density and collision frequency of microwave-resonant-cavity-produced discharges. *J. Appl. Phys.* **74**, 3724–3735 (1993).



66. Denysenko, I. B., Kersten, H. & Azarenkov, N. A. Electron energy distribution in a dusty plasma: analytical approach. *Phys. Rev. E* **92**, 033102 (2015).
67. Wang, D. Z. & Dong, J. Q. Kinetics of low pressure rf discharges with dust particles. *J. Appl. Phys.* **81**, 38–42 (1997).
68. Choi, S. J. & Kushner, M. J. A particle-in-cell simulation of dust charging and shielding in low pressure glow discharges. *IEEE Trans. Plasma Sci.* **22**, 138–150 (1994).
69. Pitchford, L. C. et al. Comparisons of sets of electron-neutral scattering cross sections and swarm parameters in noble gases: I. Argon. *J. Phys. D: Appl. Phys.* **46**, 334001 (2013).
70. Kawaguchi, S., Takahashi, K., Satoh, K. & Itoh, H. Electron collision cross section sets of TMS and TEOS vapours. *Plasma Sources Sci. Technol.* **26**, 054001 (2017).
71. Morgan, W. L., Winstead, C. & McKoy, V. Electron collision cross sections for tetraethoxysilane. *J. Appl. Phys.* **92**, 1663–1667 (2002).
72. Kurunczi, P., Koharian, A., Becker, K. & Martus, K. Dissociative excitation of tetramethylsilane (TMS) and hexamethyldisiloxane (HMDSO) by controlled electron impact. *Contributions Plasma Phys.* **36**, 723–735 (1996).
73. Sugohara, R. T., Lee, M. T., De Souza, G. L., Homem, M. G. & Iga, I. Cross sections for elastic electron scattering by tetramethylsilane in the intermediate-energy range. *Phys. Rev. A* **84**, 062709 (2011).
74. Kemaneci, E. et al. A numerical analysis of a microwave induced coaxial surface wave discharge fed with a mixture of oxygen and hexamethyldisiloxane for the purpose of deposition. *Plasma Sources Sci. Technol.* **28**, 115003 (2019).
75. Jauberteau, J. L. & Jauberteau, I. Comparison of hexamethyldisiloxane dissociation processes in plasma. *J. Phys. Chem. A* **116**, 8840–8850 (2012).

### Acknowledgements

The authors wish to thank A.B. Schrader and P. Sanders for their skilful technical support during the preparation of the experiments. This activity is co-funded by PPS-contribution Research and Innovation of the Ministry of Economic Affairs and Climate Policy (The Netherlands), and Prodrive Technologies B.V.

### Author contributions

T.J.A. drafted the manuscript; T.J.A. created the computer code for interpretation; M.I. acquired the experimental data; T.J.A., B., and J. contributed to the conception and

design of the experiment; J. supervised the project and co-authored the manuscript; all authors contributed to internal reviews of the manuscript.

### Competing interests

The authors declare no competing interests.

### Additional information

**Supplementary information** The online version contains supplementary material available at <https://doi.org/10.1038/s42005-021-00734-w>.

**Correspondence** and requests for materials should be addressed to Tim Jacobus Adrianus Staps.

**Peer review information** *Communications Physics* thanks Ranganathan Gopalakrishnan and the other, anonymous, reviewer(s) for their contribution to the peer review of this work. Peer reviewer reports are available.

**Reprints and permission information** is available at <http://www.nature.com/reprints>

**Publisher's note** Springer Nature remains neutral with regard to jurisdictional claims in published maps and institutional affiliations.



**Open Access** This article is licensed under a Creative Commons Attribution 4.0 International License, which permits use, sharing, adaptation, distribution and reproduction in any medium or format, as long as you give appropriate credit to the original author(s) and the source, provide a link to the Creative Commons license, and indicate if changes were made. The images or other third party material in this article are included in the article's Creative Commons license, unless indicated otherwise in a credit line to the material. If material is not included in the article's Creative Commons license and your intended use is not permitted by statutory regulation or exceeds the permitted use, you will need to obtain permission directly from the copyright holder. To view a copy of this license, visit <http://creativecommons.org/licenses/by/4.0/>.

© The Author(s) 2021